Improved photocatalytic and antibacterial performance of Cr doped TiO₂ nanoparticles

C. Gomez-Polo[1,2], S. Larumbe[3], A. Gil[1,2], D. Muñoz[4], L. Rodríguez Fernández[5], L. Fernández Barquín[6], A. García-Prieto[7,8], M.L. Fdez-Gubieda[8,9], A. Muela[4,8]

[1] Departamento de Ciencias, Universidad Pública de Navarra, Campus de Arrosadía, 31006 Pamplona, Spain.

[2] Institute for Advanced Materials and Mathematics (INAMAT²), Universidad Pública de Navarra, Campus de Arrosadía, 31006, Pamplona, Spain

[3] Centre of Advanced Surface Engineering, AIN, Cordovilla, 31191, Spain

[4] Departamento de Inmunología, Microbiología y Parasitología, Universidad del País Vasco UPV/EHU, 48940 Leioa, Spain

[5] SERMET, Universidad de Cantabria, 39005 Santander, Spain

[6] Departamento de CITIMAC, Universidad de Cantabria, 39005 Santander, Spain

[7] Departamento de Física Aplicada I, Universidad del País Vasco UPV/EHU, 48013 Bilbao, Spain

[8] BCMaterials, UPV/EHU Science Park, 48940 Leioa, Spain

[9] Departamento de Electricidad y Electrónica, Universidad del País Vasco UPV/EHU, 48940 Leioa, Spain

Abstract.- The effect of Cr and N doping in the adsorption capacity, photocatalytic properties and antibacterial response of TiO₂ anatase nanoparticles is analyzed. The nanoparticles (N-TiO₂, Cr-TiO₂ and Cr/N-TiO₂) were prepared by the *sol-gel* method. The structural (X-ray diffraction and TEM) and magnetic (SQUID magnetometry) characterization confirms the nanosized nature of the anatase nanoparticles and the absence of secondary phases. The enhancement of the adsorption capacity of the dye (methyl orange) on the surface of the catalysts for the Cr and Cr/N doped samples, together with the redshift of the UV-Vis absorbance spectra promote a high photocatalytic performance under visible light in these

1

nanocatalysts. The culturability and viability of the *Escherichia coli* DH5α in a medium supplemented with the nanoparticles was characterized and compared with the evolution under visible light (both without and with nanoparticles). The results show that $Cr-TiO_2$ nanoparticles under visible light display antibacterial activity that cannot be accounted by the toxicity of the nanoparticles alone. However the antibacterial effect is not observed in $N-TiO_2$ and $Cr/N-TiO_2$. The differences in the electrostatic charge (isoelectric point) and the degree of nanoparticle dispersion are invoked as the main origins of the different antibacterial response in the $Cr-TiO_2$ nanoparticles.

(*) Corresponding autor.-
Prof. Cristina Gómez-Polo
Departamento de Ciencias. Edificio de los Acebos.
Universidad Pública de Navarra. Campus de Arrosadia. 31006 Pamplona. Spain
Phone. +34-948169576; e.mail: gpolo@unavarra.es

1. **INTRODUCTION**

The access to safe drinking water is currently a major challenge worldwide. According to the World Health Organization, such access is essential to health, a basic human right and a component of effective policy for health protection. In fact, 3 in 10 people worldwide (2.1 billion) lack access to safe, readily available water at home [1] being microbial and chemicals the main hazards. In particular, *Escherichia coli* is an indicator of fecal contamination and is employed to verify water quality. Regarding chemical hazards, organic pollutants coming from different sources (e.g., food, consumer products, agricultural activities) are critical contaminants in wastewater.

Several technologies are currently employed in water treatment procedures: chemical disinfection, filters (membrane, porous ceramic or composite, granular media), solar and UV disinfection, coagulation and sedimentation. Advanced Oxidation Processes (AOPs) and the development of new adsorbents are innovative topics in the water treatment technology field [2, 3]. In the first case, AOPs are based on the generation of highly reactive oxidant radicals (mainly $\cdot$OH) for the degradation of the organic compounds. Among the AOPs, the heterogeneous photocatalysts based on semiconductor metal oxides (such as TiO_2 and ZnO) have demonstrated their efficiency in degrading a broad range of pollutants [2-8]. Regarding the development of efficient adsorbents, those characterized by high specific surface areas as activated carbons, nanoclays, zeolites, metal-organic frameworks have been widely analyzed [9-13].

It should be noted that adsorption itself plays an important role in the photodegradation response. In fact, prior to the photocatalytic process, the adsorption of the organic substrate to be decomposed on the surface of the catalyst takes place through chemical or physical interactions. Various parameters involved in this process should be assessed for the

optimization of the photocatalytic efficiency such as specific surface area, surface electrostatic charge or acid-base adsorption processes [14]. Subsequently, the related chemical redox reactions involved in the photocatalytic activity start through the absorption of light by the semiconductor generating electron/holes pairs and the formation of oxidant radicals that give rise to the latter decomposition reactions of the pollutants.

Among the semiconductor photocatalysts, TiO_2 (mainly the anatase phase) stands out due to their low particle size, larger textural properties, nontoxicity and thermal and chemical stability [15, 16]. However, the large energy band gap ($\sim$ 3.2 eV) in the UV range and its high electron-hole pair recombination rate hinder the large-scale application. Nanosized TiO_2 photocatalysts represent an active research topic that merges or combines on the one side, a highly efficient adsorption stage and, on the other, by means of doping, the activation of the ulterior photocatalytic reactions with visible light. While the adsorption optimization is associated to the nanoscale dimensions (high surface to volume ratio), the enhanced photocatalytic response in the visible range upon doping is correlated to the appearance of additional intragap energy levels. Hence, several strategies have been addressed by co-doping TiO_2 nanoparticles with metallic and nonmetallic elements in order to enhance the photocatalytic performance under visible light [4, 17 - 29]. Anionic doping, in particular nitrogen doping, has been reported to efficiently improve the photocatalytic response in the visible range. On the other side, cationic doping shows contradictory results in the literature. Particularly regarding Cr doping, although it promotes a clear redshift of the UV-Vis absorbance spectra, it does not always lead to visible light photocatalytic performance. Conversely, metal doping usually leads to the occurrence of traps for electrons and holes. Thus, photocatalytic response under metal doping is a complex phenomenon controlled by several factors such as synthesis procedure, doping level and microstructure. Particularly, maximum

photocatalytic degradation rates under visible light are found in TiO_2 nanostructures under low Cr doping (2-5%) [30-32]. Regarding N and Cr co-doping, it has been shown, both theoretically and experimentally, the occurrence of a maximum band gap narrowing in the titanium oxide semiconductor [33-36]. These results are interpreted as a consequence of the uncompensated n-p doping, enhancing the solubility of the dopants and creating intermediate electronic bands in the gap region. Despite this synergic effect, few reports analyze the photocatalytic response of these co-doped TiO_2 nanostructures under visible light [37-39].

With respect to conventional water disinfection techniques for pathogenic microorganisms, conventional chemical oxidation agents (such as chlorine, chlorine dioxide, chloramines, and ozone) are mainly employed. Due to the formation of harmful disinfection byproducts, UV technologies are proposed as an alternative disinfection technique. However, their main drawbacks are the higher cost, energy consumption and less effectiveness for UV-resistant pathogens. Thus, heterogeneous semiconductor photocatalysts are proposed for developing next-generation sustainable water disinfection systems on the basis of the generation of highly reactive species under UV-Vis irradiation. In fact, TiO_2 was firstly reported in 1985 to inactivate bacteria under UV irradiation [40]. Regarding practical purposes, the activation of the semiconductor under visible (solar) light would enable to go one step further in the development of low cost water disinfection systems. As previously described, the main limitation of titanium dioxide is related to its wide band gap. Thus, different visible-light-active photocatalytic semiconductors have been proposed as microbial agents for the removal of pathogenic bacteria: graphitic carbon nitride (g-C_3N_4) [41], Bi_2WO_6 [42], Mn-Zn ferrites [43] or CdS [44] among others. In the case of TiO_2 nanosystems, the metallic and nonmetallic doping (i.e., Ag [45], N [46]) is again proposed an efficient strategy in the development of microbial agents activated under visible light.

Accordingly, the aim of the current work is to analyze the effect of N and Cr doping on the adsorption, photocatalytic and antibacterial properties of TiO_2 nanoparticles. The physical and chemical properties of the photocatalysts, synthesized by *sol-gel* method, were comparatively analyzed employing various characterization techniques (X-ray diffraction, Transmission Electron Microscopy (TEM), Inductively Coupled Plasma Atomic Emission Spectroscopy (ICP-AES), C and N elemental analysis, Nitrogen adsorption at 77 K, Isoelectric point, UV-Vis spectrometry, SQUID magnetometry). The results indicate that the inclusion of Cr in the anatase structure leads to maximum specific surface areas, promoting an enhancement of the adsorption processes (employing methyl orange as organic dye). Both anion and cation doping give rise to a redshift of the optical absorption spectra. However, active photocatalytic response under visible light is only achieved in Cr and Cr/N doped nanoparticles. Additionally, the antibacterial activity of the nanoparticles was evaluated on *Escherichia coli* DH5α under darkness and irradiation (visible range). Surprisingly, the Cr doped sample displays the highest antibacterial efficiency under visible light irradiation. The results are interpreted in terms of the electrostatic interactions (i.e. isolectric point) and the degree of dispersion of the doped nanoparticles.

2. EXPERIMENTAL PROCEDURE

TiO_2 doped nanoparticles (N-TiO_2, Cr-TiO_2 and Cr/N-TiO_2) were synthesized by the *sol-gel* method using titanium tetraisopropoxide (TTIP) as chemical precursor [47, 48]. The hydrolysis and condensation reactions were carried out in an ethanolic solution, fixing the pH value to 2.7 using a buffer (pH = 2) and a hydrolysis rate (molar ratio of hydrolysis water and organic precursor) of 3. The temperature was kept constant at 323 K. For the preparation of Cr

doped nanoparticles, chromium nitrate ($Cr(NO_3)_3$ $9H_2O$) was used as precursor, being added to the hydrolysis water prior to its mixture with the ethanolic solution containing the TTIP. For the preparation of the nitrogen doped samples, urea was added directly and mechanically mixed with the as-prepared precursor gel (TTIP:urea equal to 1:3). Subsequently, in all cases, the gels were dried at 333 K and calcined at 623 K for 2 h. This calcination temperature was selected according the thermogravimetry analysis (complete decomposition of the organic precursor) [48].

The calcined nanoparticles were firstly characterized by X-Ray diffraction with a BRUKER D500 (step of 0.02° and time step of 20s) while the composition was analyzed by Inductively Coupled Plasma Atomic Emission Spectroscopy (ICP-AES, VARIAN VISTA MPX) and an elemental analyzer NC 2500 THERMO QUEST for Cr and N doping, respectively. The residual carbon percentage after the calcination process was also quantified through the elemental analyzer. Transmission Electron Microscopy (JEOL Jem 2100) and EDX analysis (Oxford INCA X-stream EDX spectrometer) were employed in the characterization of the nanoparticles. In order to evaluate the formation of metal (magnetic) oxide clusters under doping, SQUID magnetometry (QUANTUM DESIGN MPMS XL7) was employed to characterize the magnetic response of the samples. Owing to the outstanding role of the specific surface area in the photocatalytic response, the study of the textural properties was carried out by means of nitrogen adsorption with a Micromeritics model ASAP 2010. Moreover, the isoelectric point of the photocatalysts was evaluated with a Z SIZER model MALVERN NANO ZS ZEN 3600. Diffuse Reflectance Spectroscopy (UV-Visible spectrophotometer model PERKIN ELMER LAMBDA 950 in reflectance mode) was employed to characterize the optical properties of the samples.

The photocatalytic efficiency was assessed through the measurement of the decomposition rate of an organic substrate, methyl orange (85% purity), at a fixed pH of 2.7. This pH was selected due the best performance of titanium dioxide as photocatalysts under acidic conditions [49]. Concentrations of methyl orange of 16 mg_{dye}/l and 0.5 g_{oxide}/l for the titanium dioxide nanoparticles were employed in the photocatalytic experiments under UV (power = 6 W, monochromatic λ = 365 nm) and visible light employing a 90 W Xenon lamp with a continuous emission spectrum, very similar to sunlight (maximum emission λ = 500 - 650 nm). The degradation rate was characterized through the quantification of the relative concentration of the methyl orange at various times employing UV-Vis spectrophotometry (LAN OPTICS 1104 RS) through the relative changes in the absorbance at λ = 500 nm (maximum absorbance wavelength of the methyl orange at the employed pH). In order to discern the effect of the adsorption from the photocatalytic reactions, similar experiments were performed in darkness.

The antibacterial performance of the NPs was evaluated on *Escherichia coli* DH5α. The strain was grown up to stationary phase at 37 °C and shaking (250 rpm.) in Luria Bertani Broth. The cells were harvested by centrifugation at 5500 rpm. and 4 °C for 15 min and washed three times in sterile phosphate buffered saline (PBS). Finally, bacterial suspensions were prepared in sterile Milli-Q water (non-supplemented and supplemented with 100-400 μg/ml of nanoparticles) to reach a density around 10^5 cell/ml. The bacterial suspensions were incubated for 5-8 h, at 298 K and slight shaking (90 rpm.), both in darkness and illuminated conditions. For each experimental condition, samples were periodically collected to determine the total number of cells and the number of viable and culturable bacteria. The viable bacteria were estimated as bacteria with intact cytoplasmic membranes (MEMB+) using the Live/Dead BacLight^{TM} kit (Invitrogen). The samples stained with the kit were analyzed by flow cytometry

on a Beckman Coulter Gallios cytometer. The number of culturable bacteria (expressed as colony forming units, CFU) was evaluated by the spread plate method, on Luria Bertani Agar incubated 24 h at 310 K. All the results presented below are the means of at least three replicated experiments. The illumination system was composed of Philips fluorescent tubes TL5 HO 54W/965 and TL5 HO 54W/840, which emit in the range 360–740 nm with emission peaks at 440, 540/60, 620/60 nm. The irradiance was approximately 125W/m^2.

3. RESULTS AND DISCUSSION

3.1. Material characterization

Firstly, the crystallographic structure of the calcined samples analyzed through X-ray diffraction, shows broad peaks identified to the anatase phase (see Figure 1).
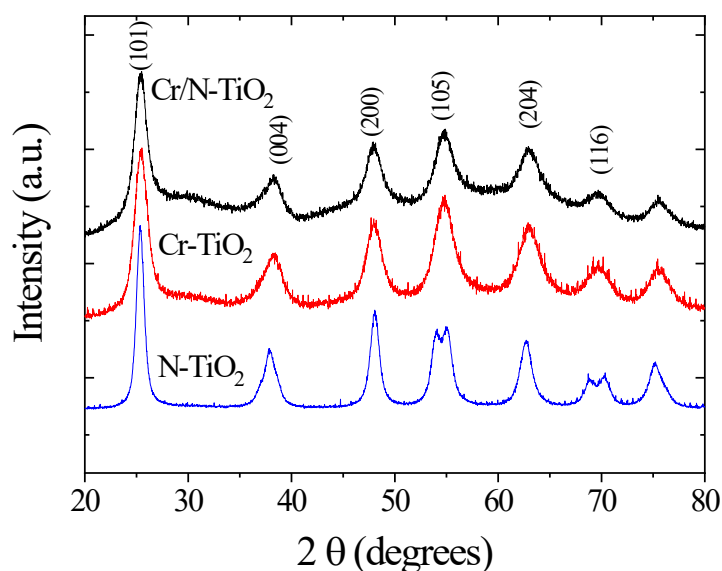

Figure 1: X-ray diffraction patterns for the calcined nanoparticles. Patterns have been shifted up for clarity. Miller indices are assigned to the diffraction peaks.

No remarkable change in the lattice parameter with the doping is clearly detected. Mean crystallite sizes, estimated simply using the Scherrer equation at the maximum intense peak (101) reflection, range from 6 nm for the Cr and Cr/N co-doped samples up to 9 nm in the N doped sample (see Table I). No other peaks related to secondary phases (i.e., Cr clusters, Cr oxides or Cr-Ti oxide phases) can be detected in the X-ray diffraction patterns.

Table I: Mean crystalline size $<d>$, and C, Cr and N concentrations (% in weight) in the calcined nanoparticles.

Sample	$<d>$ (nm)	C (%)	N (%)	Cr (%)
N-TiO$_2$	9.4	0.20	0.40	--
Cr-TiO$_2$	5.8	0.04	--	5.7
Cr/N-TiO$_2$	6.0	0.19	0.19	5.2

Regarding the composition of the calcined samples, the concentration of C, Cr and N content is also summarized in Table I. A maximum carbon concentration of 0.2 % in weight is found associated to the decomposition of the organic precursors after calcination. While N concentration ranges between 0.2-0.4 % weight, Cr concentration is nearly constant around 5% in the Cr doped samples. Differences on the final nitrogen concentration are detected as a consequence of the possible inhomogeneity of nitrogen distribution in the sample due to the mechanical mixing of urea in the as-prepared gel. Furthermore, the competition between Cr and N to react with Ti^{4+} could give rise to the different amount of N in the anatase structure when Cr is absent."
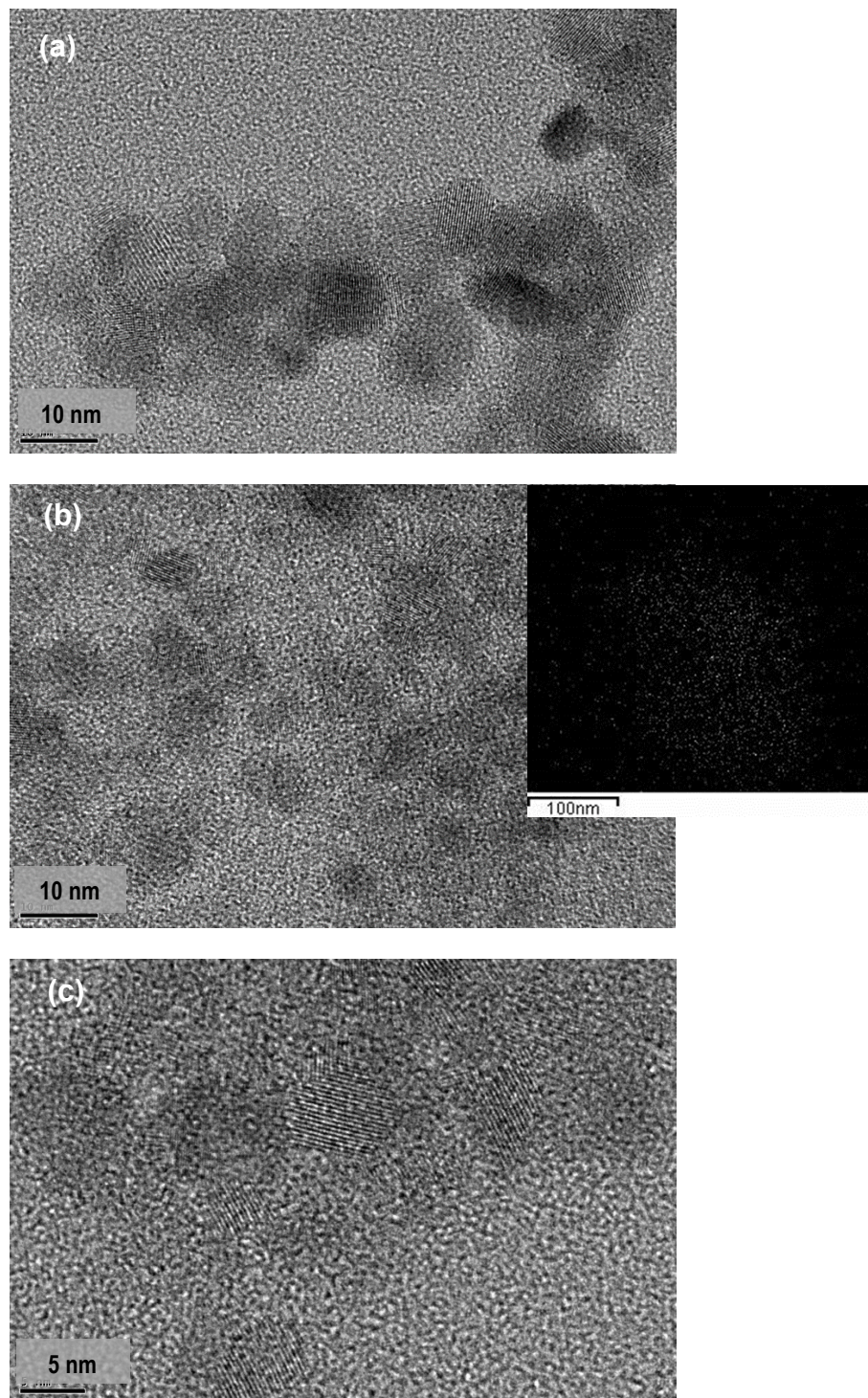
Figure 2: TEM images for the (a) N-TiO$_2$, (b) Cr-TiO$_2$ and (c) Cr/N-TiO$_2$ calcined nanoparticles. Atomic planes can be identified in some of the nanoparticles revealing their good crystallinity. Inset (b): Cr mapping by EDX measurements.

Figure 2 shows TEM images for the (a) N-TiO$_2$, (b) Cr-TiO$_2$ and (c) Cr/N-TiO$_2$ calcined samples. The nanoparticles display a nearly spherical shape with mean grain diameters similar to the crystalline sizes displayed in Table I. Furthermore, as previously deduced from the X-ray diffraction results, a slight decrease in the mean nanoparticle size is observed with the Cr doping. For these Cr doped samples, EDX mapping (see as an example Cr-TiO$_2$ in the inset of Figure 2b) confirms a homogeneous distribution of Cr, with an equally distributed inclusion of the cation on the anatase phase and the absence of Cr secondary phases.

Although no secondary phases can be directly inferred from the previous structural analysis it may happen they could be present in very low quantities. If those phases were magnetic, they could be disclosed by high sensitivity SQUID magnetometry. Hence, the magnetic characterization was employed as an additional tool to check the occurrence of metal oxide phases in the Cr-doped samples. First, it should be noted that the calcined samples display at room temperature linear hysteresis loops, characteristic of a paramagnetic behavior. In order to evaluate the magnetic nature of these doped samples, the *Zero Field Cooled-Field Cooled* thermal-dependent magnetization (*ZFC-FC*) curves were obtained at an applied magnetic field of 50 Oe (see Figure 3). Firstly, the magnetization *M(T)* increases continuously when reducing the temperature. This *M(T)* shape is typical of a paramagnet. In addition, the absence of irreversible behavior between the *ZFC-FC* curves further confirms the paramagnetic response in the analyzed temperature range (5 – 300 K). In fact, the analysis of the Curie Weiss law (

$\chi = \dfrac{C}{T + T_N}$, *C* constant; T_N Néel temperature), namely χ^1 versus temperature, *T*, (see Figures

3b and c) indicates the antiferromagnetic nature of the Cr doped samples with T_N = 4 and 12 K for Cr and Cr,N doped nanoparticles, respectively.
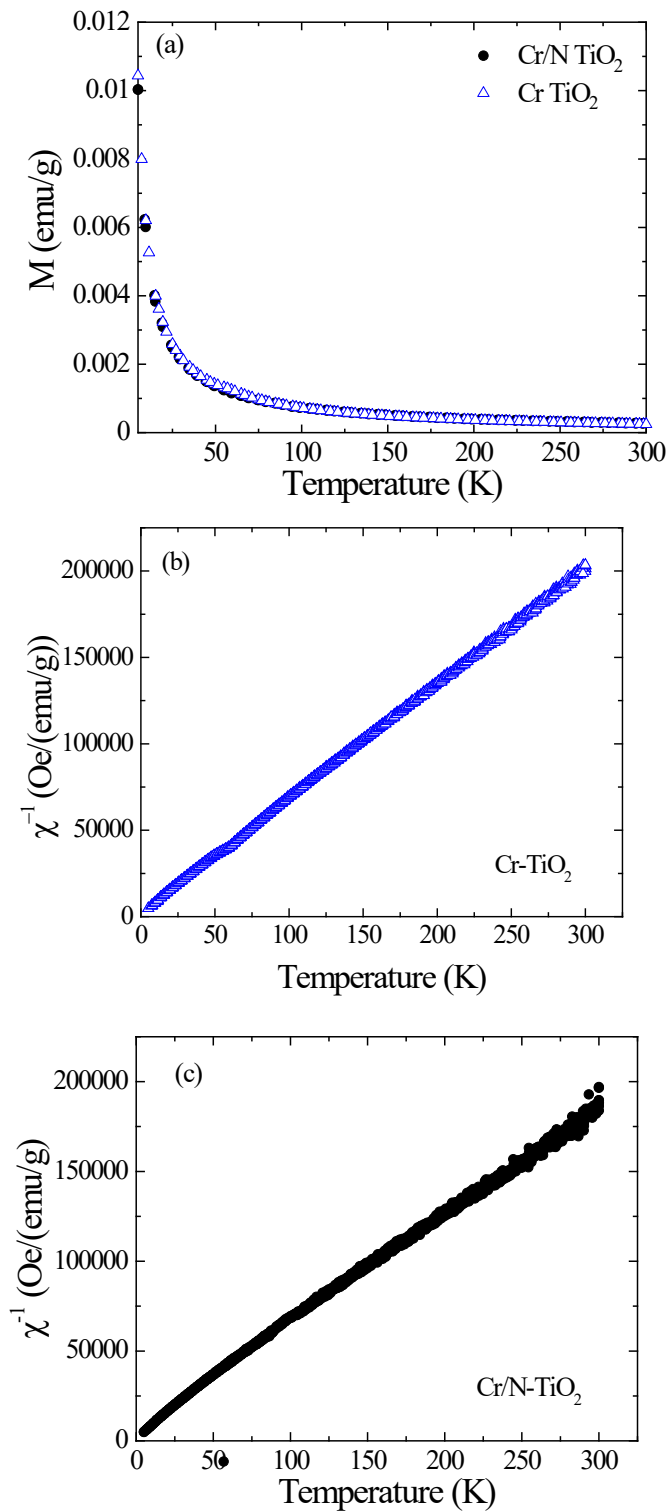
Figure 3: (a) *ZFC-FC* magnetization curves of the Cr and Cr/N doped nanoparticles; Inverse of the magnetic susceptibility, χ^{-1}, versus temperature for (b) Cr-TiO$_2$ and (c) Cr/N-TiO$_2$ nanoparticles.

Taking into account that the Néel temperature of antiferromagnetic Cr oxides in bulk is much higher (386 K and 308 K for CrO_2 and Cr_2O_3, respectively [44]), the occurrence of minor secondary magnetic phases can be disregarded supporting the homogenous distribution of the Cr^{3+} ions in the anatase TiO_2 phase. Similar antiferromagnetic behavior is found in other metallic doped TiO_2 nanostructures [18] explained in terms of the exchange coupling between the metal ions through the oxoanions of the lattice [50].
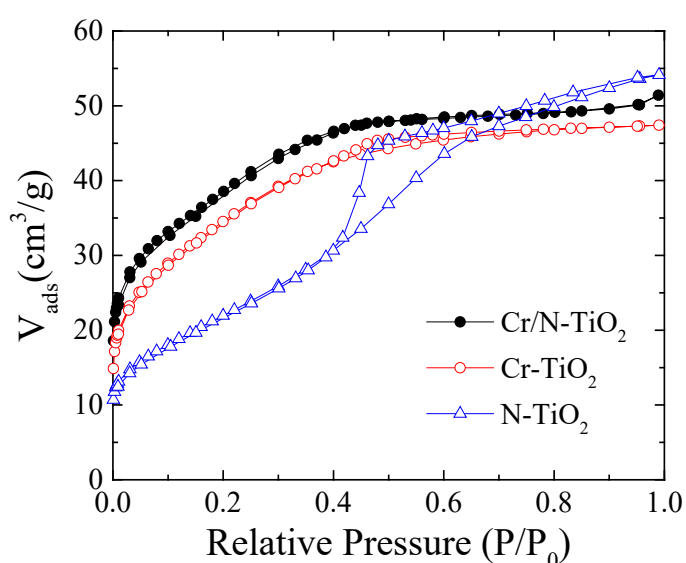

Figure 4: Nitrogen adsorption-desorption curves at 77 K for the doped TiO_2 calcined samples.

Regarding the characterization of the texture of the doped titanium dioxide nanoparticles, the adsorption-desorption of nitrogen is shown in Figure 4. It is noticeable a different behavior between the samples although the synthesis procedure was similar for all of them. This result clearly indicates the effect of the doping element on the final textural properties. Specifically for the N doped sample, a curve type IV with a hysteresis type H_2 ascribed to a mesoporous material is observed [51]. Cr and Cr/N-TiO_2 nanoparticles display the typical adsorption curve type I related to a microporous material. In these cases, the presence

of hysteresis is not observed. The estimated *BET* specific surface area for each sample is summarized in Table II. It can be concluded that the Cr doping gives rise to a clear increase in the specific surface (around 130 m^2/g) in comparison with the values in N-TiO$_2$ (80 m^2/g).

However, the pore distribution is quite small in all the samples within the limit between microporous and mesoporous regimes, with a mean pore size around 4 nm for N doped sample and around 2 nm for the Cr and Cr/N doped samples. Maximum and minimum values of *BET* surface area and pore diameter, respectively, for Cr doped samples should be ascribed to lower mean grain crystalline sizes (see Table I) [39]. As it will be shown, the specific surface area plays a dominant role in the adsorption stage controlling the photocatalytic response of the nanocatalysts.

Table II: Textural properties (*BET* surface and pore diameter), Isoelectric point (*IEP*) and band gap energy, E_g, for the doped titanium dioxide nanoparticles.

Samples	BET surface (m^2/g)	Pore diameter (nm)	IEP	E_g (eV)
N-TiO$_2$	80	4.0 -4.5	2.60	1.6
Cr-TiO$_2$	125	2.2 - 2.5	3.30	1.1
Cr/N-TiO$_2$	137	2.3 - 2.5	1.90	1.5

Due to the outstanding role of electrostatic interactions in the first stages of the adsorption process of the organic substrate on the photocatalyst surface, the isoelectric point (*IEP*) was characterized. The isoelectric point is defined as the pH at which the Zeta Potential achieves a net value of zero. Thus, higher values of pH give rise to a negative surface charge and on the opposite, lower pH values than *IEP* lead to a positive surface charge. The Zeta Potential of the set of nanoparticles as a function of pH is presented in Figure 5. The introduction of doping elements on the anatase structure with various oxidation state and ionic

radii, gives rise to a distortion of the crystal structure and to changes in the *IEP*. In this case, notice that the Cr doped sample displays a higher *IEP* value than the adjusted pH during the photocatalytic degradation of the methyl orange (pH = 2.7). However, an opposite trend (*IEP* < 2.7) is observed with the nitrogen doping (see Table II). The Cr doping of TiO_2 nanoparticles brings about an increase of the *IEP* value with respect to those of both nitrogen doped TiO_2 samples (N-TiO_2 and Cr/N-TiO_2). One possible explanation could be the different oxidation state of Cr^{3+} and N^{3-} and thus the corresponding different charge imbalance generated in the surface of the nanoparticles. The introduction of nitrogen ions in the anatase structure promotes the generation of oxygen vacancies, a decrease of the coordination of Ti^{4+} ions with oxygen anions. Therefore, there is a generation of a positively charged surface giving as a result Lewis acidity and in consequence the observation of lower *IEP* values. [52]. On the other side, the introduction of chromium ions (Cr^{3+}) in the TiO_2 lattice substituting Ti^{4+} could give rise to the occurrence of Brönsted acidity and higher values of *IEP*.
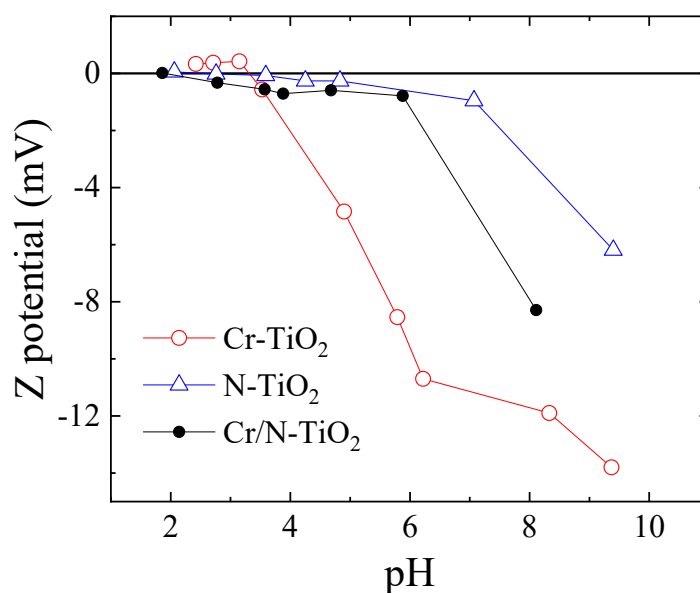

Figure 5: Zeta potential curves versus pH for the doped calcined samples.

In relation to the photocatalysis response and the design of highly effective wastewater photocatalysts, a relevant aspect is the activation of the catalytic reactions under visible light irradiation. As previously indicated, both metallic (Cr) and non metallic (N) doping leads to a reduction of the effective optical band gap energy (E_g) as a consequence of the existence of intermediate energetic levels in the band gap region. In order to depict the normalized absorbance (UV-Visible spectra), with respect to the wavelength, the so-called Kubelka-Munk function was calculated for each sample with the reflectance measured spectra.
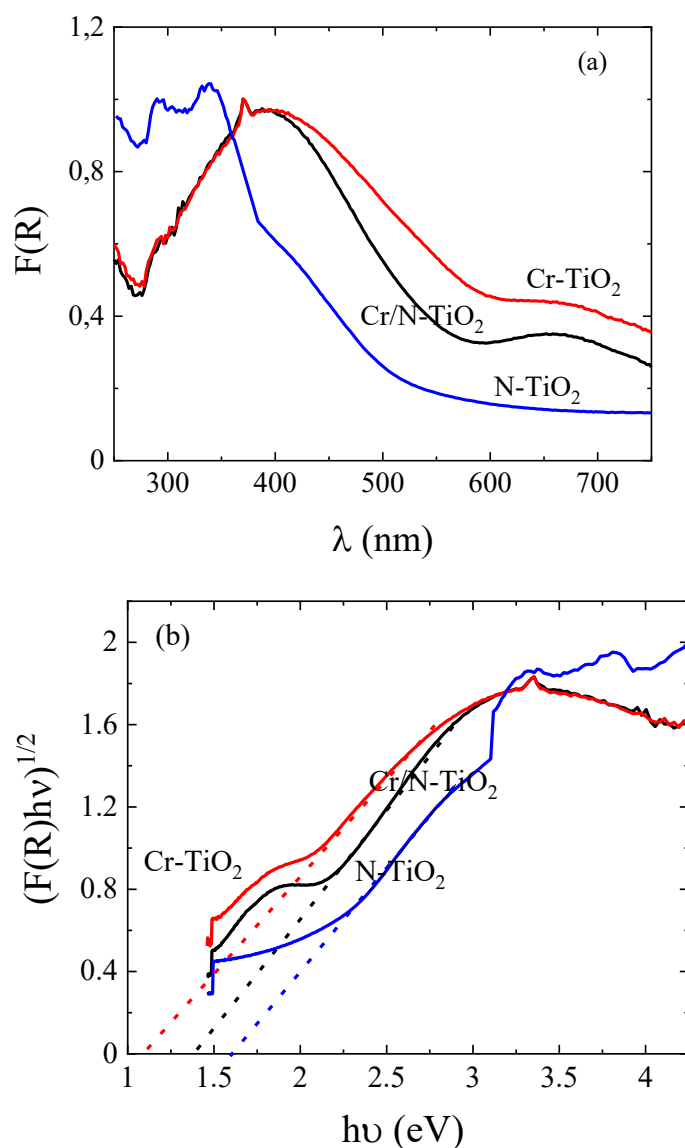

Figure 6: (a) UV-Vis spectra (Kubelka-Munk function $F(R)$ versus wavelength, λ, and (b) Tauc plots $((F(R)h\upsilon)^{1/2}$ versus $h\upsilon$ for the doped TiO$_2$ nanoparticles.

The Kubelka-Munk function $\left(F(R) = \dfrac{(1-R)^2}{2R} \right)$, being R the reflectance, as a function

of the wavelength, λ, for the analyzed samples is presented in Figure 6. A clear redshift

(decrease in E_g) is obtained in the doped samples in comparison to the TiO$_2$ anatase ($E_g \approx 3$ eV

[47]). Furthermore, for the Cr doped samples, an absorption band in the higher wavelengths

region (≈ 600 nm) is detected and related to the electronic transitions d-d of the Cr^{3+} ions in the

octahedral sites [53, 54].

The absorption coefficient, α, proportional to the Kubelka-Munk function can be

expressed as $\alpha = A(h\nu - E_g)^n / h\nu$ where A is a constant, ν the frequency and $n = 2$ for TiO$_2$

(indirect transitions). Accordingly, the so-called Tauc plot $(F(R)h\nu)^{1/2}$ vs. $h\nu$) can be

employed for the estimation of E_g (see Figure 6b) through the linear extrapolation for $h\nu \to$

0 (see Table II). As shown in previous reports [18, 21, 30, 53], a clear diminution of the effective

band gap energy is found upon Cr and N doping. However, in the present case the co-doping

with Cr and N does not significantly enhance the band gap narrowing with respect to the values

estimated in the Cr and N doped samples.

3.2.   *Adsorption and photocatalytic characterization*

After the previous structural, magnetic and optical characterization, the photocatalytic

response of the nanoparticles was checked through the degradation of the substrate (methyl

orange) under UV and visible (Vis) radiation. In a first stage, the effect of the adsorption of the

methyl orange on the photocatalysts surface was analyzed through the measurement of the

substrate concentration (C) as a function of time (t) under dark (C_0: initial concentration). As

the results included in Figure 7a show, there is a clear difference between N and the Cr and Cr/N TiO$_2$ samples. While the adsorption process can be disregarded in the N-TiO$_2$ sample, a remarkable decrease in C/C_0 is found under dark for the Cr and Cr/N doped samples. This effect cannot be only ascribed to the differences in the electrostatic surface charge of the catalysts. As it was previously shown, the isoelectric point (*IEP*, see Table II) for the case of the N and the Cr/N doped samples, is below the pH of the medium during the experiment. By contrast, *IEP* for the Cr doped TiO$_2$ sample is higher than the pH of the solution. Hence, the effect of the electrostatic charge on the adsorption response should be disregarded. Otherwise, the specific surface areas would play the dominant role in the adsorption process related to the mesoporous and microporous character of the oxides. As the results included in Table II show, those samples with highest specific surface areas (Cr and Cr/N doped nanopowders) display the largest changes in the dye concentration under dark.

Similar experiments were carried out irradiating the solutions employing a monochromatic UV and Xenon light (see Figures 7b and 7c, respectively). Light irradiation was applied with the initiation of C/C_0 versus time measurement (simultaneously with adsorption). N-TiO$_2$ sample exhibits the highest degradation rate under UV radiation. However, regarding practical purposes, that is, efficient photocatalysts under visible light, this sample is not able to lead to significant changes in the dye concentration employing the Xe light.

With respect to the Cr and Cr/N doped photocatalysts, small differences are detected in the evolution of C/C_0 in darkness and under UV irradiation (minimum C/C_0 around 0.3 and 0.4 for Cr and Cr/N samples, respectively).
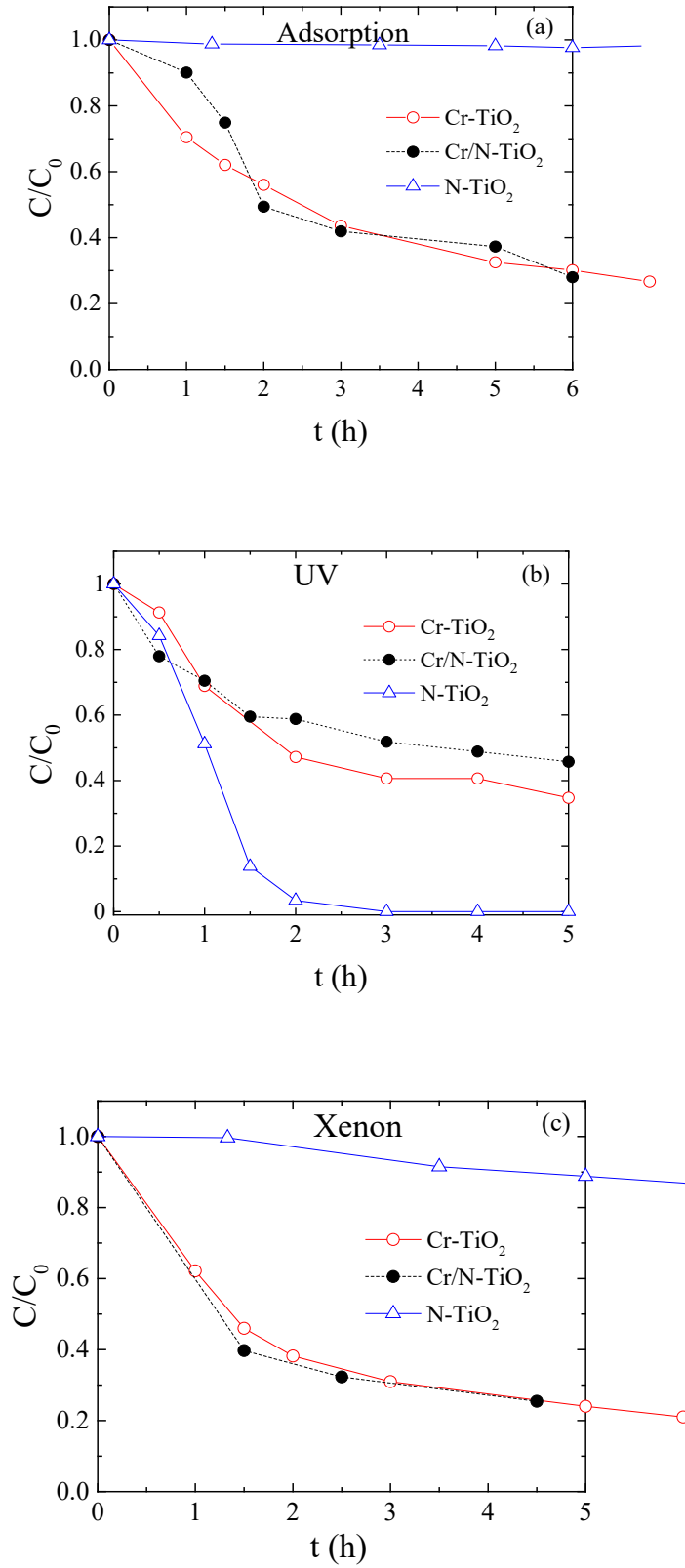
Figure 7: Evolution of the dye concentration (C/C_0) versus time (t) under different radiation conditions employing (a) adsorption (darkness), (b) UV and (c) Xenon lamps.

Nevertheless, a slight enhancement in the degradation rate is detected in both samples under Xe (visible light) lamp in spite of the low power of the lamp employed in the experiments (minimum $C/C_0 \approx 0.2$). This behavior supports the contribution of the band gap narrowing in the photocatalytic process (redshift) in these Cr doped photocatalysts. "However, N-TiO$_2$ nanoparticles lead to a reduced substrate degradation under visible light, in spite of the similar E_g values found for the three analyzed photocatalysts. In fact, if Figure 6a is observed with further detail, N-TiO$_2$ nanoparticles display a reduced optical absorption for wavelengths around the maximum of the Xe lamp irradiation ($\lambda = 500 - 650$ nm), that certainly remark the differences with the Cr doped samples.

3.3.Bioassay (antibacterial characterization)

As previously introduced, it is well documented that the photocatalytic performance of TiO$_2$ nanoparticles under UV-Vis light involves the formation of free radicals that can activate decomposition reactions in biological entities, a property that has been exploited for microbial disinfection applications. According to the previous characterization, the synthesized nanocatalysts, in particular Cr-TiO$_2$ and Cr/N-TiO$_2$, nanoparticles are suitable candidates for antimicrobial applications under visible light. In this line, the performance of the doped nanoparticles was addressed as antibacterial agents employing *Escherichia coli* as indicator.

Figure 8 shows the survival of *Escherichia coli* in a time period of 5-6 h i) under visible light irradiation (*L*); ii) in darkness in a medium supplemented with 100 μg/ml nanoparticles((a) N-TiO$_2$, (b) Cr-TiO$_2$ and (c) Cr/N-TiO$_2$) (*NP*); and iii) under visible light in a medium supplemented with 100 μg/ml nanoparticles (*LNP*). Survival is measured by the time evolution of the number of culturable cells (with ability to divide) or culturability.
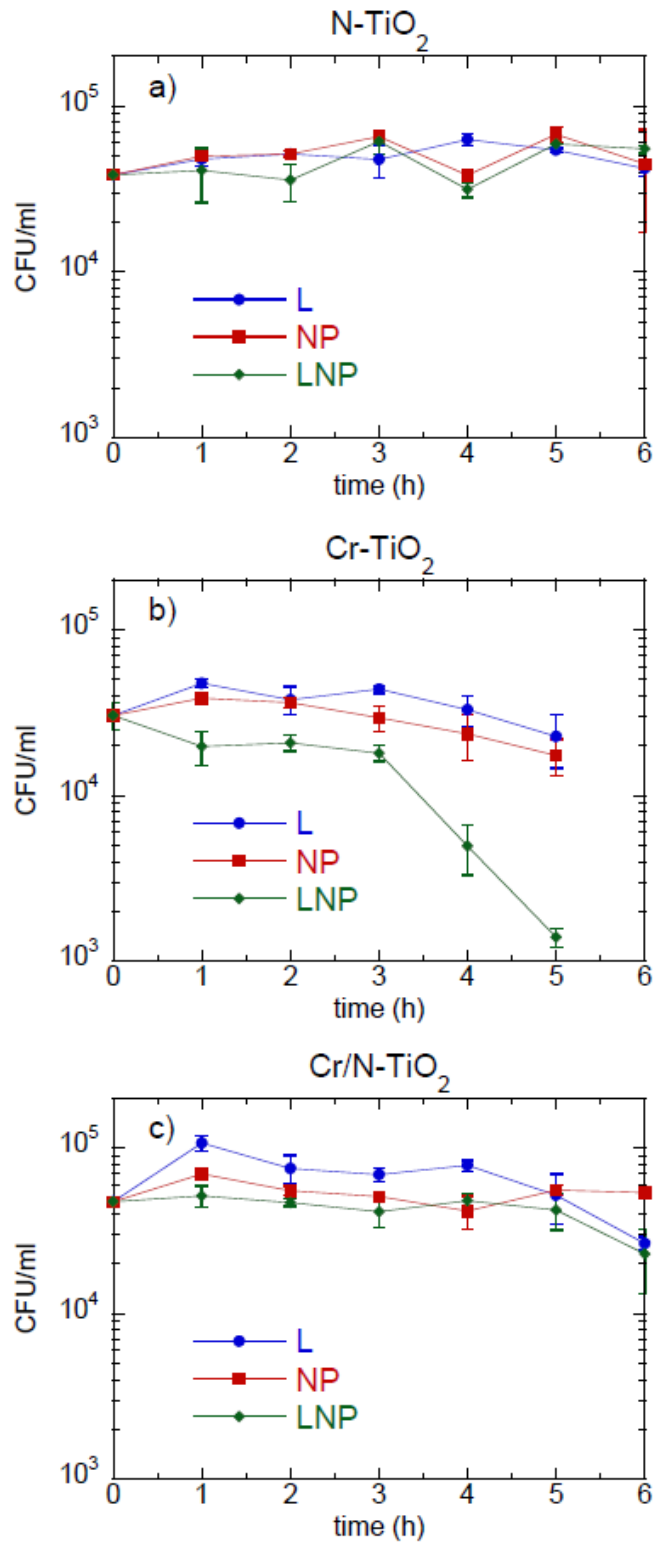
Figure 8: Culturability of *E. coli* under visible light (L), in darkness in a medium supplemented with 100 µg/ml nanoparticles (a) N-TiO₂, b) Cr-TiO₂, c) Cr/N-TiO₂) (NP), and under visible light and in the presence of nanoparticles (LNP). The number of culturable bacteria is shown as number of colony forming units (CFU).

For N and Cr/N-TiO$_2$ NPs, the culturability of the bacterial populations in darkness does not change in 6 h when nanoparticles are present and no differences are observed between the illuminated systems with and without nanoparticles. These results indicate that bacterial division is not affected either by the presence of nanoparticles, or by the combination of visible light and NPs.

A different scenario is observed for Cr-TiO$_2$ nanoparticles. In this case, the nanoparticles slightly affect culturability, and when both visible light and NPs are present (*LNP*), the culturability decreases drastically after 3 h. This result reveals a certain toxigenic power in Cr-TiO$_2$ and suggests that visible light could be activating a photocatalytic response in the Cr-TiO$_2$ nanoparticles that hinders bacterial division. Aimed to assess whether the decrease of culturability is accompanied by a bactericidal effect in this sample, an additional study has been conducted in which the longer term effects on both bacterial culturability and viability (the ratio of live cells to total cells, being live cells those whose cytoplasmic membrane is intact) have been measured. These additional studies have been performed using a higher concentration of Cr-TiO$_2$ NPs (200 µg/ml) because, as shown in Figure 9 at this concentration the effects of the combination of light and NPs on culturability are significantly enhanced. Interestingly, using a higher nanoparticle concentration (400 µg/ml) the culturability does not change appreciably with respect to the values observed for 200 µg/ml.
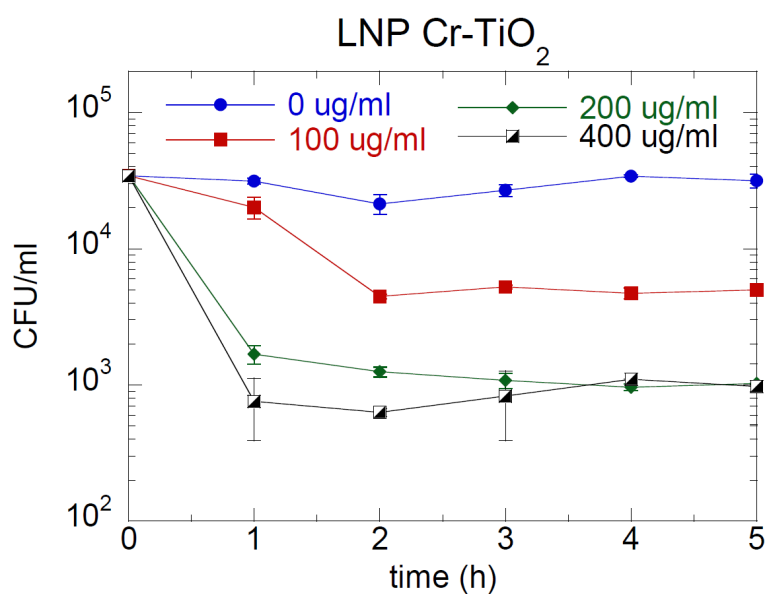
Figure 9: Culturability of *E. coli* under visible light and in the presence of increasing concentrations of Cr-TiO₂ NPs (0, 100, 200 and 400 µg/ml). The number of culturable bacteria is shown as number of colony forming units (CFU).
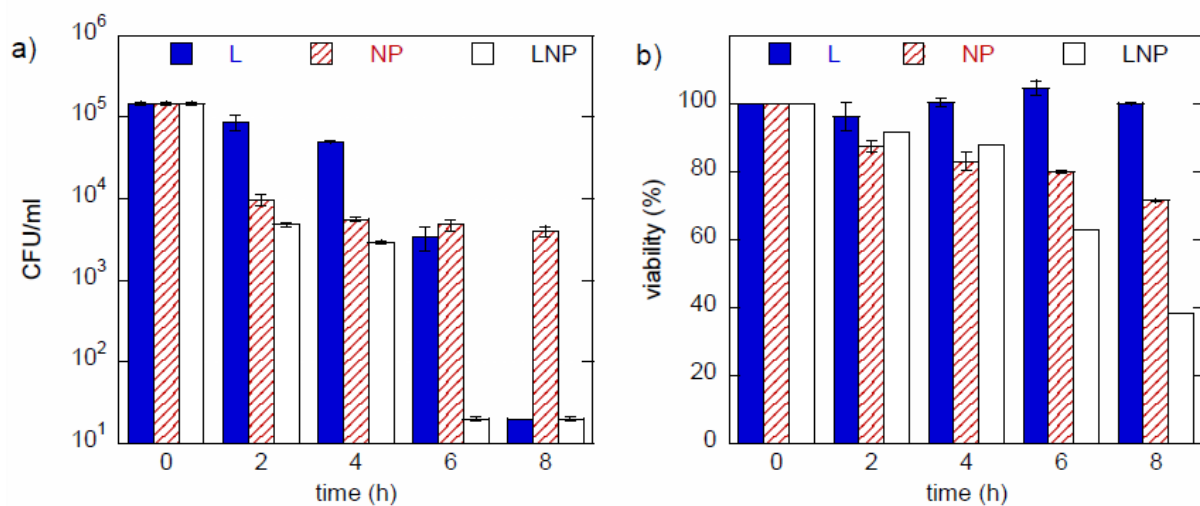

Figure 10: a) Culturability and b) viability of *E. coli* under visible light (L), in darkness and in the presence of 200 µg/ml of Cr-TiO₂ NPs (NP), and under visible light and in the presence of NPs (LNP). The number of culturable bacteria is estimated by plate count and shown as number of colony forming units (CFU).

Finally, Figure 10 shows the longer term effects on both the culturability and the viability of *E. coli* under visible light in Cr-TiO$_2$ nanoparticles (200 µg/ml) and the combination of visible light and nanoparticles. As shown in Figure 10a, visible light (*L*) affects the culturability, which decreases slowly up to 6 h but drops drastically at 8 h. However, visible light does not affect the viability, as shown in Figure 10b. Therefore, it can be concluded that visible light hinders the cell division but does not kill the cells.

Regarding the effect of the nanoparticles (NP in Figure 10), both the culturability and the viability of *E. coli* decrease slowly with time. After 8 h the number of culturable cells is reduced around 1.5 orders in magnitude but the viability of the bacterial population remains at 70%, indicating that there is some toxicity associated to the NPs.

The most important effect occurs when both visible light and NPs are combined (*LNP* in Figure 10). In this case, the culturability decreases slowly up to 4 h, but drops drastically after 6 h. At this time point, the number of culturable cells is reduced around 4 orders in magnitude and it is 200 times lower than when only visible light (*L*) or nanoparticles (*NP*) are present. This confirms that the combination of light and nanoparticles hinders cell division drastically, much more than both effects separately, as observed previously in Figure 8b. Interestingly, the drop in the culturability observed after 6 h is accompanied by a less steep drop in the viability, which remains about 63% at 6 h and goes down to 38% at 8 h. Moreover, the viability is substantially lower than the viability when only NPs are present (80% at 6 h and 71% at 8 h). This indicates again that the combination of visible light and NPs has an antibacterial activity that cannot be accounted for the toxicity of the nanoparticles alone. This antibacterial activity should be then attributed to the photocatalytic activity of the Cr-TiO$_2$ NPs triggered by the visible light and the result is not only bacteriostatic but also bactericidal.

However, as Figure 8 displays, N and Cr/N TiO$_2$ nanoparticles do not affect the bacteria either in darkness or under visible light. Taking into account that the bactericidal effect is associated to the photocatalytic response of the nanoparticles, the negligible activation of the N-TiO$_2$ sample under visible light would explain this result (see Figure 7c). However, as this figure also reflects, both Cr and Cr/N doped samples display similar photocatalytic degradation under Xe lamp. Furthermore, no significant differences in the structural (grain size and textural features), magnetic and optical properties are found between these Cr doped nanoparticles (with the exception of a slight decrease in the band gap energy for the Cr-TiO$_2$ nanoparticles). As previously discussed, the main difference lies in the isolectric point (*IES*) and the different electrostatic charge distribution as a function of the pH of the media. As Figure 5 shows Cr-TiO$_2$ nanoparticles show a much lower Z-potential (~-12 mV) than N and Cr/N TiO$_2$ (~-2 mV) at the pH (6,5-7) at which the bioassays were carried out. Indeed, the Z-potential is an indication of the degree of dispersion in the medium and can be employed to characterize the electrostatic charge of the nanoparticle surface [55]. The higher Z-potential (smaller in absolute value) of N and Cr/N-TiO$_2$ nanoparticles at the pH of the bacterial tests would indicate a higher aggregation, and thus a lower effective surface exposed to the light. Therefore, a reduction in the photocatalytic effect is expected to lead to negligible antibacterial response in these nanoparticles under light irradiation.

4. CONCLUSIONS

The photocatalytic response of N, Cr and Cr/N doped TiO$_2$ nanoparticles has been analyzed employing methyl orange as substrate. The nanoparticles, synthesized by a *sol-gel* method, display anatase structure with mean grain sizes between 6 and 9 nm. Chromium doping

(Cr and Cr/N- TiO$_2$) gives rise to a reduction in the mean grain size and an increase in the specific surface area of the photocatalysts. These effects mainly contribute to the photocatalytic response, reflected in a high adsorption of the dye on the photocatalysts surface. A clear redshift (decrease in the energy band gap) of the optical absorption spectra is found in the doped (N, Cr and N/Cr) nanoparticles associated to the occurrence of additional intragap energy levels. In spite of the band gap narrowing, only the Cr doped nanoparticles (Cr and Cr/N-TiO$_2$) display moderate photocatalytic response under visible light. Furthermore, the antibacterial activity of the nanoparticles was evaluated on *Escherichia coli* under darkness and irradiation (visible range). The results show a clear antibacterial effect of the Cr-TiO$_2$ nanoparticles under visible light irradiation that is mainly associated to the higher degree of dispersion as a result of the minimum negative Z-potential (enhancement of electrostatic interactions). Therefore, the combination of high specific surface area (high adsorption rate), photocatalytic response, and antibacterial effect under visible light, makes Cr-TiO$_2$ nanoparticles effective photocatalysts and microbial agents for wastewater technologies.

References

1.- www.who.int/water_sanitation_health/water-quality/en/

2.- C. Santhosh, V. Velmurugan, G. Jacob, S. K. Jeong, A. N. Grace, and A. Bhatnagar, *Role of nanomaterials in water treatment applications: A review*, Chem. Eng. J. 306 (2016) 1116–1137 . https://doi.org/10.1016/j.cej.2016.08.053.

3.- K. K. Chenab, B. Sohrabi, A. Jafari, S. Ramakrishna, *Water treatment: functional nanomaterials and applications from adsorption to photodegradation*, Mater. Today Chemistry, 16 (2020) 100262. https://doi.org/10.1016/j.mtchem.2020.100262

4.- A. Gil, A.M. García, M. Fernández, M.A. Vicente, B. González-Rodríguez, V. Rives, S.A. Korili, *Effect of dopants on the structure of titanium oxide used as a photocatalyst for the removal of emergent contaminants*, J. Ind. Eng. Chem. 53 (2017) 183-191. https://doi.org/10.1016/j.jiec.201.

5.- B. Pant, M. Park, S.J. Park, *Recent advances in TiO$_2$ films prepared by sol-gel methods for photocatalytic degradation of organic pollutants and antibacterial activities*, Coatings 9 (2019) 613. https://doi.org/10.3390/coatings9100613.

6.- X. Yu, X. Lin, W. Feng, W. Li, *Enhanced catalytic performance of a bio-templated TiO$_2$ UV-Fenton system on the degradation of tetracycline*, Appl. Surf. Sci. 465 (2019) 223-231 https://doi.org/10.1016/j.apsusc.2018.09.145.

7.- T. Yang, J. Peng, Y. Zheng, X. He,Y. Hou, L. Wu, X. Fu, *Enhanced photocatalytic ozonation degradation of organic pollutants by ZnO modified TiO$_2$ nanocomposites,* Appl. Catal. B-Environ. 221 (2018) 223-234. https://doi.org/10.1016/j.apcatb.2017.09.025.

8.- J. Lan, B. He, C. Haw, M. G. Khana, R. Zheng, S. Guo, J. Zhao, Z. Wang, S. Huang, S. Li, J. Kang, *Band engineering of ZnO/Si nanowire arrays in Z-scheme heterojunction for efficient dye photodegradation,* Appl. Surf. Sci. 529, 1 (2020) 147023. https://doi.org/10.1016/j.apsusc.2020.147023.

9.- A. Gil, F.C.C. Assis, S. Albeniz, S.A. Korili, *Removal of dyes from wastewaters by adsorption on pillared clays*, Chem. Eng. J. 168 (2011) 1032-1040. https://doi.org/10.1016/j.cej.2011.01.078.

10.- A. Gil, N. Taoufik, A.M. García, S.A. Korili, *Comparative removal of emerging contaminants from aqueous solution by adsorption on an activated carbon*, Environ. Technol. 40 (2019) 3017-3030. https://doi.org/10.1080/09593330.2018.1464066.

11.- T. Rasheed, A. A. Hassan, M. Bilal, T. Hussain, K. Rizwan, *Metal-organic frameworks based adsorbents: A review from removal perspective of various environmental contaminants from wastewater*, Chemosphere 259 (2020) 127369. https://doi.org/10.1016/j.chemosphere.2020.127369.

12.- M. Van den Bergh, A. Krajnc, S. Voorspoels, S. Rodrigues Tavares, S. Mullens, I. Beurroies, G. Maurin, G. Mali, D. E. De Vos, *Highly Selective Removal of Perfluorinated Contaminants by Adsorption on All-Silica Zeolite Beta* Angew. Chem. Int. Ed. 59 (2020) 14086–14090 https://doi.org/10.1002/anie.202002953.

13.- A. Mojiri, J. L. Zhou, B. Robinson, A. Ohashi, N. Ozaki, T. Kindaichi, H. Farraji, M. Vakili, *Pesticides in aquatic environments and their removal by adsorption methods,* Chemosphere 253 (2020) 126646. https://doi.org/10.1016/j.chemosphere.2020.126646.

14.- A. O. Ibhadon, P. Fitzpatrick, *Heterogeneous Photocatalysis: Recent Advances and Applications*, Catalysts 3, 1 (2013) 189-218. https://doi.org/10.3390/catal3010189.

15.- K. Nakata, A. Fujishima, *TiO$_2$ photocatalysis: Design and applications*, J. Photochem. Photobiol. C-Photochem. Rev. 13 (2012) 169-189. https://doi.org/10.1016/j.jphotochemrev.2012.06.001.

16.-J. Schneider, M. Matsuoka, M. Takeuchi, J. Zhang, Y. Horiuchi, M. Anpo, D.W. Bahnemann, *Understanding TiO$_2$ Photocatalysis: Mechanisms and Materials,* Chem. Rev. 114 (2014) 9919-9986. https://doi.org/10.1021/cr5001892.

17.- X. Dan, K. L. Yao, G. Y. Gao, and L. Yang, *Electronic and optical properties of N-doped, Co-doped as well as N,Co-codoped rutile TiO$_2$*, J. Magn. Magn. Mater. 335 (2013) 118–124. 10.1016/j.jmmm.2013.02.010.

18.-S. Larumbe, M. Monge, C. Gómez-Polo, *Comparative study of (N, Fe) doped TiO2 photocatalysts*, Appl. Surf. Sci., 327 (2015) 490–497.

19.- Y. Cao, Z. Xing, M. Hu, Z. Li, X. Wu, T. Zhao, Z. Xiu, S. Yang, W. Zhou, *Mesoporous black N- TiO$_2$ hollow spheres as efficient visible light driven photocatalysts,* J. Catal. 356 (2017) 246-254. 10.1016/j.jcat.2017.10.023.

20.- D. Li, Y. Liu, H. Liu, Z. Li, L. Lu, J. Liang, Z. huang, W. Li, *Nitrogen-doped carbon enhanced mesoporous TiO$_2$ in photocatlytic remedation of organic pollutants*, Res Chem Intermed (2018). doi.org/10.1007/s11164-018-3531-9.

21.- E. D. Toe, W. Kurniawan, E.G. Mariquit, H. Hinode, *Synthesis of N-doped mesoporous TiO$_2$ by facile one-step solvothermal process for visible light photocatalytic degradation of organic pollutant*, J. Environ. Chem. Eng. 6 (2018) 5125-5134. 10.1016/j.jece.2018.08.005.

22.- A. Garg, T. Singhania, A. Singh, S. Sharma, S. Rani, A. Neogy, S.R. Yadav, V.K. Sangal, N. Garg, *Photocatalytic Degradation of Bisphenol-A using N, Co Codoped TiO$_2$ Catalyst under Solar Light,* Sci Rep 9 (2019) 765. https://doi.org/10.1038/s41598-018-38358-w.

23.- P.A. Ochoa Rodriguez, G.A, Pecchi, S.G. Casuscelli, V.R. Elias, G.A. Eimer, *A simple synthesis way to obtain iron-doped TiO$_2$ nanoparticles as photocatalytic surfaces,* Chem. Phys. Lett.732 (2019) 136643. https://doi.org/10.1016/j.cplett.2019.136643.

24.- K. Singh, S. Harish, J. Archana, M. Navaneethan, M. Shimomura, Y. Hayakawa, *Investigation of Gd-doped mesoporous TiO$_2$ spheres for environmental remediation and energy applications*, Appl. Surf. Sci. 489 (2019) 883-892. https://doi.org/10.1016/j.apsusc.2019.05.253.

25.- M.-C. Wu, T.-H. Lin, K.-H., Hsu, J.-F Hsu, *Photo-induced disinfection property and photocatalytic activity based on the synergistic catalytic technique of Ag doped TiO$_2$ nanofibers* Appl. Surf. Sci. 484 (2019) 326-334. https://doi.org/10.1016/j.apsusc.2019.04.028.

26.- T. Iihoshi, T. Ohwaki, J.J.M. Vequizo, A. Yamakata, A. *Improvement of photocatalytic activity under visible-light irradiation by heterojunction of Cu ion loaded WO3 and Cu ion loaded N-TiO$_2$*, Appl. Catal. B-Environ.248 (2019) 249-254. 10.1016/j.apcatb.2019.01.046.

27.- X. Yang, V. Salles, M. Maillard, Y.V. Kaneti, M. Liu, C. Journet, X. Jiang, Y. Liu, A. Brioude, *Fabrication of Au functionalized TiO$_2$ nanofibers for photocatalytic application*, J. Nanopart. Res. 21 (2019)160. https://doi.org/10.1007/s11051-019-4600-8.

28.- D.M. Tobaldi, L. Lajaunie, M. Lopez Haro, R.A.S. Ferreira, M. Leoni, M.P.Seabra, J.J. Calvino, L.D. Carlos, J.A. Labrincha, *Synergy of Neodymium and Copper for Fast and Reversible Visible-light Promoted Photochromism, and Photocatalysis, in Cu/Nd-TiO$_2$ Nanoparticles,* ACS Appl. Energy Mater. 2019, 2 (2019) 3237-3252. https://doi.org/10.1021/acsaem.9b00084.

29.- Y. Yu, J. Xia, C. Chen, H. Chen, J. Geng, H. Li*, One-step synthesis of a visible-light driven C@N–TiO$_2$ porous nanocomposite: Enhanced absorption, photocatalytic and photoelectrochemical performance,* J. Phys. Chem. Solids 136 (2020) 109169. 10.1016/j.jpcs.2019.109169.

30.- C. Diaz-Uribe, W. Vallejo, W. Ramos, *Methylene blue photocatalytic mineralization under visible irradation on TiO$_2$ thin films doped with chromium,* Appl. Surf. Sci. 319 (2014) 121-127. https://doi.org/10.1016/j.apsusc.2014.06.157.

31.- S.N. R. Inturi, M. Suidan, P.G. Smirniotis, *Influence of synthesis method of the Cr-TiO$_2$ catalyst for visible light liquid phase photocatlysis and their stability*, Appl. Catal. B-Environ. 180 (2016) 351-361. 10.1016/j.apcatb.2015.05.046.

32.- R. Senthil Kumar, B. Gnanavel, A. Jegatheesan, *Microwave assited synthesis and characterization of pure and Cr doped TiO$_2$ with improved photo-efficiency*, J. Mater. Sci.-Mater. Electron. 29 (2018) 6501-6510.

33.- W. Zhu, X. Qiu, V. Iancu, Z.-Q. Chen, H. Pan, W. Wang, N.M. Dimitrijevic, T. Rajh, H.M. Meyer III, M. Parans Paranthaman, G.M. Stocks, H.H. Witering, B. Gu, G. Eresm Z. Zhang, *Band gap narrowing of titanium dioxide semiconductors by noncompensated anion-catopn codoping for enhanced visble-light photoactivity*, Phys. Rev. Lett. 103 (2009) 226401. 10.1103/PhysRevLett.103.226401.

34.- M. Chuiodi, C.Parks Cheney, P. Vilmercati, E. Cavalieri, N. Mannella, H.H. Weitering, L. Gavioli, *Enhanced dopant solubility and visible-light asorption in Cr-N codoped TiO2 nanoclusers*, J. Phys. Chem C 116 (2012) 311-318. https://doi.org/10.1021/jp208834n.

35.- C.Parks Cheney, P. Vilmercati, E.W. Martin, M. Chuiodi, L. Gavioli, M. Regmi, G. Eres, T.A. Callcott, H.H. Weitering and N. Mannella, *Origins of electronic band gap reduction in Cr/N codoped TiO$_2$*, Phys. Rev. Lett. 112 (2014) 036404. 10.1103/PhysRevLett.112.036404.

36.- G. H. Jaffari, A. Tahir, N. Zafar Alo, A. Ali, U. S. Qurashi, *Effect of Cr-N codoping on structural phase transition, Raman modes,and optical properties of TiO$_2$ nanoparticles*, J. Appl. Phys. 123 (2018) 161541. https://doi.org/10.1063/1.5003448.

37.- M.E. Kurtoglu, T. Logenbach, K. Sohlberg, Y. Gogotsi, *Strong coupling of Cr and N in Cr-N doped TiO$_2$ and its effect on photcatalytic activity*, J. Phys. Chem. C 115 (2011) 17392-17399. https://doi.org/10.1021/jp2026972.

38.- W.-C. Lu, H.-D. Nguyen, C.-Y. Wu, K.-S. Chang, M. Yoshimura, *Modulation of physical and photocatalytic properties of (Cr,N) codoped TiO$_2$ nanorods using soft solution processing*, J. Appl. Phys. 115 (2014) 144305. https://doi.org/10.1063/1.4871200.

39.- J. Fan, Z. Zhao, J. Wang, L. Zhu, *Synthesis of Cr,N-doped titania nanotubes and their visble-light-driven photocatalytic properties*, Appl. Surf. Sci. 324 (2015) 691-697. https://doi.org/10.1016/j.apsusc.2014.11.018.

40.- T. Matsunaga, R. Tomoda, T. Nakajima, H. Wake, *Photoelectrochemical sterilization of microbial cells by semiconductor powders*, FEMS Microbiol. Lett. 29, 1–2 (1985) 211-214. https://doi.org/10.1093/femsle/fnaa091.

41.- C. Zhang, Y. Li, D. Shuai, Y. Shen, W. Xiong, L. Wang, *Graphitic carbon nitride (g-C$_3$N$_4$)-based photocatalysts for water disinfection and microbial control: A review*, Chemosphere 214 (2019) 462-479. https://doi.org/10.1016/j.chemosphere.2018.09.137.

42.- M. Karbasi, F. Karimzadeh, K. Raeissi , S. Rtimi, J. Kiwi, S. Giannakis, C. Pulgarin, *Insights into the photocatalytic bacterial inactivation by flower-like Bi$_2$WO$_6$ under solar or visible light, through in situ monitoring and determination of Reactive Oxygen Species (ROS)*, Water 12 (2020) 1099. 10.3390/w12041099.

43.- M.I.A.Abdel Maksoud, Gharieb S.El-Sayyad, Ahmed M.El-Khawaga, M.Abd Elkodousd, A.Abokhadra, Mohamed A.Elsayed, Mohamed Gobara, L.I. Soliman, H.H. El-Bahnasawy, A.H. Ashou, *Nanostructured Mg substituted Mn-Zn ferrites: A magnetic recyclable catalyst for outstanding photocatalytic and antimicrobial potentials*, J. Hazard. Mater.399, 15 (2020) 123000. https://doi.org/10.1016/j.jhazmat.2020.123000.

44.- F. Qureshi, M. Nawaz, S. Rehman, S. A. Almofty, S. Shahzad, V. Nissapatorn, M. Tahah, *Synthesis and characterization of cadmium-bismuth microspheres for the catalytic and photocatalytic degradation of organic pollutants, with antibacterial, antioxidant and*

cytotoxicity assay J. Photochem. Photobiol. B-Biol. 202 (2020) 111723. https://doi.org/10.1016/j.jphotobiol.2019.111723.

45.- M.-C. Wu, T.-H. Lin, K.-H. Hsu, J.-F. Hsu, *Photo-induced disinfection property and photocatalytic activity based on the synergistic catalytic technique of Ag doped TiO_2 nanofibers*, Appl. Surf. Sci. 484, 1 (2019) 326-334. https://doi.org/10.1016/j.apsusc.2019.04.028.

46.- L. Zhou, M. Cai, X. Zhang, N. Cui, G. Chen, G.-y, Zou, *In-situ nitrogen-doped black TiO_2 with enhanced visible-light-driven photocatalytic inactivation of Microcystis aeruginosa cells: Synthesization, performance and mechanism*, Appl. Catal. B-Environ. 272 (2020) 119019. https://doi.org/10.1016/j.apcatb.2020.119019.

47.- C. Gómez-Polo, S. Larumbe, M. Monge, *Room temperature ferromagnetism and sbsorption red-shift in nitrogen-doped TiO_2 nanoparticles*, J. Alloy. Compd. 612 (2014) 450-455. 10.1016/j.jallcom.2014.05.178.

48.- S. Larumbe, C. Gómez-Polo, *Magentic properties of N and (Cr,N)- doped TiO2 nanoparticles,* IEEE Trans. Mag. 51 (2015) 2400904. 10.1109/TMAG.2015.2446997.

49.- Y. Zhang, J. Wan, Y. Ke, *A novel approach of preparing TiO_2 films at low temperature and its application in photocatalytic degradation of methyl orange*, J. Hazard. Mater. 177 (2010) 750. https://doi.org/10.1016/j.jhazmat.2009.12.095.

50.- J.M.D. Coey, A.P. Douvalis, C.B. Fitzefgerald, M. Venkatensan, *Ferromagnetims in Fe-doped SnO*, Appl. Phys. Lett. 84 (2004) 1332. https://doi.org/10.1063/1.1650041.

51.- A. Gil, *Análisis textural de sólidos porosos mediante adsorción física de gases*, Universidad Pública de Navarra (2019). ISBN: 978-84-9769-349-3.

52.- M. Sahu, K. Suttiponparmit, S. Suvachittanont, T. Charinpanitkul, P. Biswas, *Characterization of doped TiO_2 nanoparticle dispersions*, Chem. Eng. Sci. 66 (2011) 3482-3490. https://doi.org/10.1016/j.ces.2011.04.003.

53.- Y.-H. Peng, G.-F. Huang, W.-Q. Huang, *Visible-light absorption and photocatlytic activity on Cr-Doped TiO_2*, Adv. Powder Technol. 23 (2012) 8-12. https://doi.org/10.1016/j.apt.2010.11.006.

54.- B. Choudhury, A. Choudhury, *Structural, optical and ferromagnetic properties of Cr-Doped TiO2 nanoparticles*, Mater. Sci. Eng. B Solid-State Mater. Adv. Technol. 178 (2013) 794-800. https://doi.org/10.1016/j.mseb.2013.03.016.

55.- W. W. Wilson, M. M. Wade, S. C. Holman, F. R. Champlin, *Status of methods for assessing bacterial cell surface charge properties based on zeta potential measurements*, Journal of Microbiological Methods 43 (2001) 153–164.